

# Visualizing inversion results with rock physics templates

Brian Russell<sup>1</sup>

<sup>1</sup> Hampson-Russell, A CGG GeoSoftware Company, Calgary, Alberta, [brian.russell@cggs.com](mailto:brian.russell@cggs.com)

## ABSTRACT

In this report, I discuss several new approaches for linking rock physics to the seismic reservoir characterization process. I will first discuss a deterministic rock physics approach and show how we can project the results of rock physics modeling onto a cross-plot of  $V_P/V_S$  ratio versus P-impedance that has been extracted from the results of simultaneous pre-stack seismic inversion. From this cross-plot interpretation we can then project the results directly onto the seismic volume itself. Having identified the hydrocarbon zone using this deterministic approach I will then discuss a statistical clustering and classification approach applied to the data cross-plot which will allow us to develop a probabilistic interpretation of the extent of the hydrocarbon anomaly. This approach will go beyond the normal approach using bivariate Gaussian pdf functions and will introduce the concept of mixture-Gaussian pdfs. As with the deterministic method, the pdf classification functions can then be projected onto the seismic volume. I will illustrate the various approaches with examples from a gas sand example in Alberta.

## INTRODUCTION

Today, most geoscientists have an array of tools available to perform seismic reservoir characterization. However, the complexity of these tools increases year by year, and can be overwhelming at times. In this paper, I will show how to improve the user-friendliness of the reservoir characterization process using both deterministic and statistical approaches, and will illustrate these methods with examples from a shallow gas sand prospect in Alberta.

Before getting into the details of the two methods, let me first describe the reservoir geophysics workflow shown in Figure 1. As seen in this figure, the starting point for the workflow is the data itself, where the well data is shown on the left of the plot and the seismic data is on the right of the plot. Ideally, the well data includes P-wave velocity,  $V_P$ , S-wave velocity,  $V_S$ , and density,  $\rho$ , so that adequate rock physics and synthetic modeling can be done. However, if only P-wave velocity and density is available, Gassmann modeling can be used to create the S-wave velocity (the Gassmann equation will be discussed in the next section). Many rock physics models are available, from unconsolidated gas sand modeling through complex fractured carbonate modeling. In the next section, we will review an approach to modeling unconsolidated gas sands that was initially proposed by Ødegaard and Avseth (2003).

The next step, synthetic seismic modeling, first involves extracting a wavelet from the seismic data and then tieing the zero-offset synthetic seismogram to the

stacked seismic data. After this, pre-stack synthetics can be created and compared to the pre-stack seismic data. In this paper, we will not discuss synthetic tying and modeling, but will assume that these steps have been done.

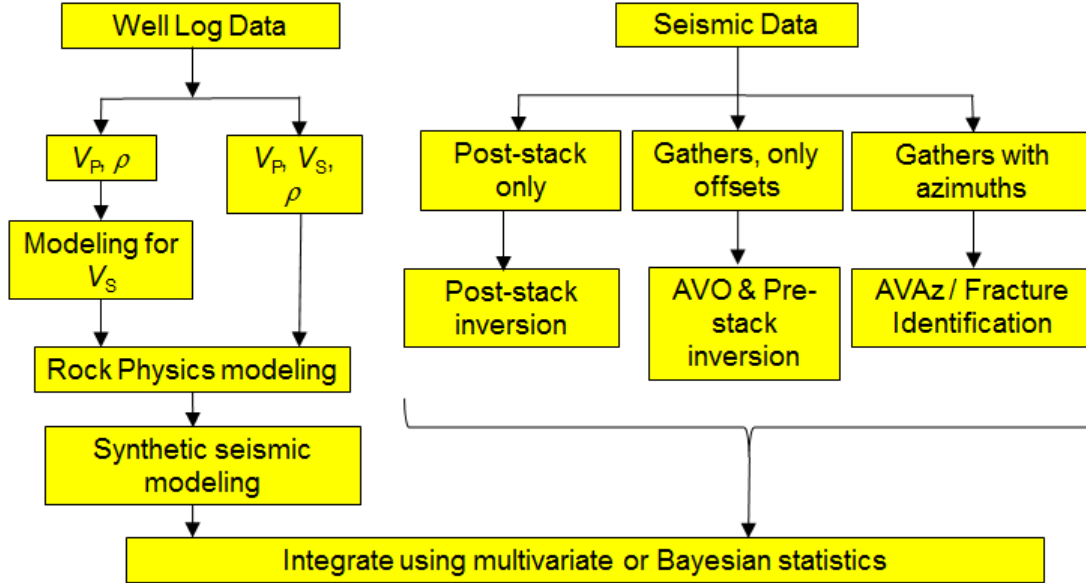


Figure 1: A reservoir geophysics workflow.

Next, we come to the seismic data input stream shown in Figure 1. A fundamental decision on how to proceed will come with the type of data available in the project. If only post-stack data is available, you will be limited to post-stack inversion, in which the result is P-impedance, the product of density and P-wave velocity. If pre-stack data with offset or angle information is available, then full pre-stack inversion can be implemented, which results in P-impedance, S-impedance and density (from which other elastic volumes like  $V_P/V_S$  ratio, Poisson's ratio, Young's modulus, lambda-mu, lambda-rho and  $V_P$  and  $V_S$  can be generated). In this talk, we will apply pre-stack inversion to our gas sand example, and will show how the results picked interactively from various lithological and fluid zones on the inverted dataset can be displayed on a cross-plot and integrated with a rock physics template.

As also shown in Figure 1, if the pre-stack data has been recorded with a full range of azimuths, AVAz analysis can be applied and fracture identification can be performed. However, on the dataset used in this study, azimuth information was not available.

In the final step shown in Figure 1, note that all of our rock physics and seismic attributes can be integrated using either multivariate or Bayesian statistics. In this study, the last section will show how Bayesian statistics, using both bivariate Gaussian and mixture Gaussian pdf functions, can be used to assign a probability distribution to each lithological or fluid zone picked from the seismic data and integrated with the rock physics model. This allows us to quantify the probability of finding a hydrocarbon zone in other parts of the survey.

First, we will look at the well log data used in the study, and cross-plot this data in a form that will be used throughout the analysis.

## THE COLONY WELL DATA

The dataset used in this study is a shallow gas sand over the Colony formation in southern Alberta. Figure 2 shows the well logs recorded in a well drilled into this gas sand. Note that the gas sand is roughly ten metres thick between depths of 632 m and 642 m. The P-wave sonic log and density logs shown in Figure 2 were recorded in-situ, whereas the S-wave sonic log was created using Castagna's equation (Castagna et al., 1985) outside the gas sand zone, and Gassmann fluid replacement modeling within the gas sand zone.

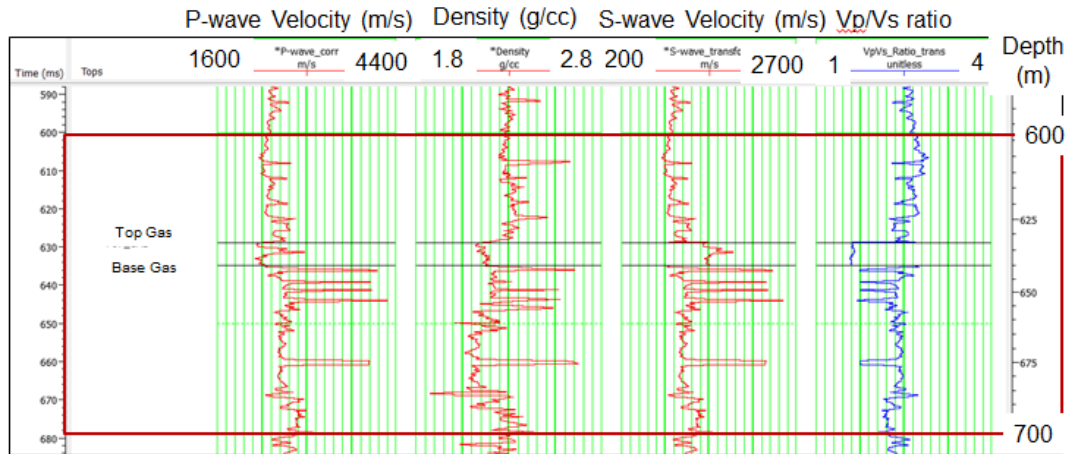


Figure 2: The well log suite for the producing well in the Colony gas sand.

Castagna's equation is given by

$$V_S = a + bV_P \quad (1)$$

If other wells in the area contain  $V_P$  and  $V_S$  curves, the coefficients in equation 1 can be obtained through a local regression. However, since no observed  $V_P$  and  $V_S$  curves are available in this area, the coefficients used here are the inverse of those found in Castagna et al. (1985), which are  $a = -1172$  m/s and  $b = 0.862$ .

The Gassmann equation is given by

$$\frac{K_{sat}}{K_m - K_{sat}} = \frac{K_{dry}}{K_m - K_{dry}} + \frac{K_f}{\phi(K_m - K_f)}, \quad (2)$$

where  $K_{sat}$  is the saturated bulk modulus,  $K_{dry}$  is the dry bulk modulus,  $K_m$  is the mineral bulk modulus and  $\phi$  is the porosity of the reservoir rock, and  $K_f$  is the bulk modulus of the reservoir fluid.

To estimate the  $K_{dry}$  value, we used the method proposed by Greenberg and Castagna (1992), which involved the following iterative scheme:

1. Estimate the brine-filled P-wave velocity using an initial guess.
2. Compute the S-wave velocity from the regression line given in equation 1.
3. Perform Gassmann fluid substitution with the values from steps 1 and 2 to compute the P-wave velocity for the  $S_w < 1$  case. This requires estimates of the moduli and density of each component.
4. Based on the error between the measured and computed P-wave velocities (for  $S_w < 1$ ), go back to step 1 and perturb the estimate of the brine-filled P-wave velocity.
5. Iterate until the in-situ saturated P-wave velocities agree.

The fluid bulk modulus  $K_{fl}$ , is computed by the Reuss average given by

$$\frac{1}{K_{fl}} = \frac{S_w}{K_w} + \frac{S_{gas}}{K_{gas}} + \frac{S_{oil}}{K_{oil}}, \quad (3)$$

where in this case we set  $S_w = S_{gas} = 0.5$  and found the values of the bulk moduli using the equations giving in Batzle and Wang (19--).

We can then compute each new saturated bulk modulus value by re-arranging equation 2 to give

$$K_{sat} = K_m \frac{x}{1+x}, \quad (3)$$

where  $x = \frac{K_{dry}}{K_m - K_{dry}} + \frac{K_{fl}}{\phi(K_m - K_{fl})}$ , and varying the values of  $\phi$  (the porosities are computed using the density log in Figure 1).

Once we have computed the dry rock bulk and shear moduli at different porosities, we can use the Gassmann equation (equation 7) to model the saturated rock properties. Gassmann's theory predicts that the shear modulus is independent of fluid content, or

$$\mu_{sat} = \mu_{dry}. \quad (4)$$

Finally, we plug the new values of the bulk and shear moduli into the equations for P and S-wave velocity in the saturated, porous reservoir, given by

$$V_{P\_sat} = \sqrt{\frac{K_{sat} + \frac{4}{3}\mu_{sat}}{\rho_{sat}}}, \text{ and} \quad (5)$$

$$V_{S\_sat} = \sqrt{\frac{\mu_{sat}}{\rho_{sat}}}, \quad (6)$$

where the density values can be taken from the measured density log. Note that the  $V_P/V_S$  ratio log shown in Figure 1 can now be computed over both the wet and gas zones, and the P-impedance log (not shown in Figure 1) can be computed by multiplying the P-wave sonic by the density log.

Now we can analyze the zone between 600 and 700 m by cross-plotting the  $V_P/V_S$  ratio log against the P-impedance log, as shown in Figure 3.

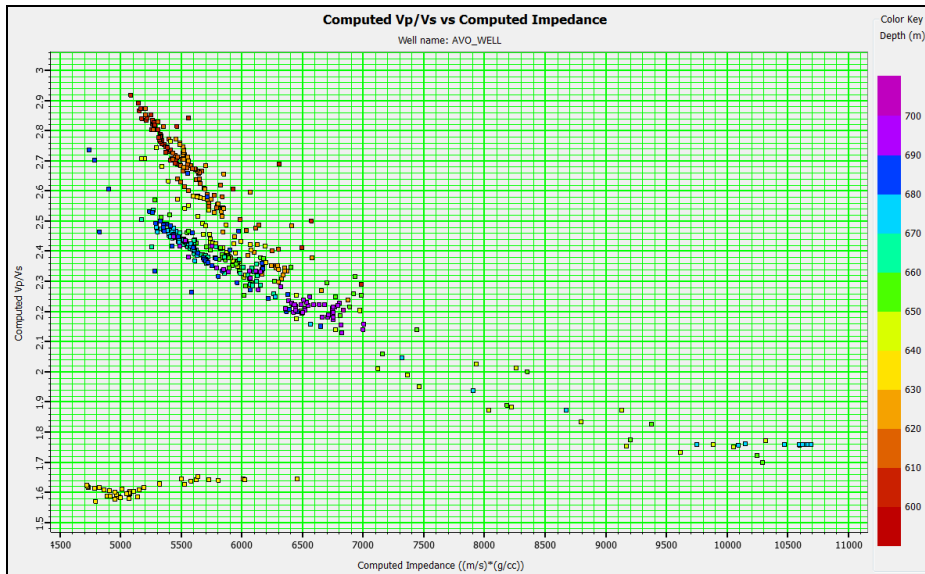


Figure 3: Cross-plotting the well log data shown in Figure 2, where the vertical axis represents  $V_P/V_S$  ratio and the horizontal axis represents P-impedance, the product of density and P-wave velocity.

Note that the cross-plot shown in Figure 3 displays a number of obvious clusters of points. These clusters can be analyzed statistically using the automatic  $K$ -means with Mahalanobis (or statistical) distance algorithm (Russell, 2003). Figure 4 shows the results of running this algorithm using five clusters.

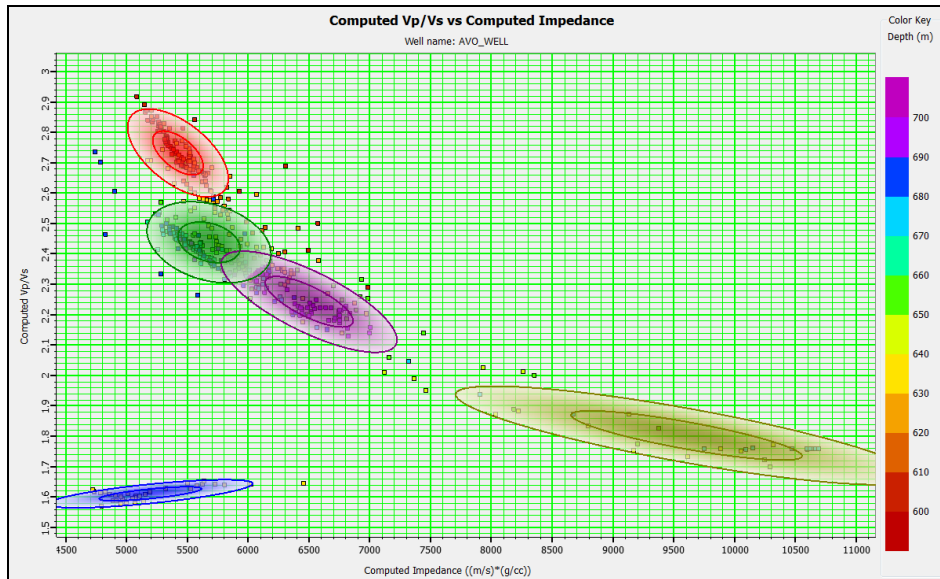


Figure 4: Here we have performed automatic clustering using statistical K-means and found 5 clusters.

However, the key question in Figure 4 is how to interpret these five automatically picked clusters. In the next section we will discuss a rock physics template deterministic method which allows us to do such an interpretation.

## THE ØDEGAARD/AVSETH ROCK PHYSICS TEMPLATE

Ødegaard and Avseth (2003) presented a technique for the interpretation of elastic inversion results using what they called the rock physics template, or RPT, approach. In this method, they compute a theoretical template consisting of values of  $V_P/V_S$  ratio versus acoustic impedance ( $\rho V_P$ ) and compare this template to results derived from both well logs and the inversion of pre-stack seismic data. To compute the values of velocity ratio and acoustic impedance, Ødegaard and Avseth (2003) compute  $K_{dry}$  and  $\mu_{dry}$  as a function of porosity,  $\phi$ , using Hertz-Mindlin contact theory (Mindlin, 1949) and the lower Hashin-Shtrikman bound (Hashin and Shtrikman, 1963). The authors also incorporate the critical porosity method for the computation of the porous and solid phases. The bulk modulus computation is given as

$$K_{dry} = \left[ \frac{\phi/\phi_c}{K_{HM} + (4/3)\mu_{HM}} + \frac{1-\phi/\phi_c}{K_m + (4/3)\mu_{HM}} \right]^{-1} - \frac{4}{3}\mu_{HM}, \quad (7)$$

and the shear modulus computation is given as

$$\mu_{dry} = \left[ \frac{\phi/\phi_c}{\mu_{HM} + z} + \frac{1-\phi/\phi_c}{\mu_m + z} \right]^{-1} - z, \quad (8)$$

where  $HM$  is an abbreviation of Hertz-Mindlin,  $K_{HM} = \left[ \frac{n^2(1-\phi_c)^2 \mu_m^2}{18\pi^2(1-\nu_m)^2} P \right]^{\frac{1}{3}}$ ,  $\mu_{HM} = \frac{5-4\nu_m}{5(2-\nu_m)} \left[ \frac{3n^2(1-\phi_c)^2 \mu_m^2}{2\pi^2(1-\nu_m)^2} P \right]^{\frac{1}{3}}$ ,  $z = \frac{\mu_{HM}}{6} \left( \frac{9K_{HM} + 8\mu_{HM}}{K_{HM} + 2\mu_{HM}} \right)$ ,  $P$  = effective pressure,  $K_m$  and  $\mu_m$  are the mineral bulk and shear moduli,  $n$  = the number of contacts per grain,  $\nu_m$  is the mineral Poisson's ratio and  $\phi_c$  is the high porosity end-member.

The saturated density can be computed from the equation

$$\rho_{sat} = \rho_m(1-\phi) + \rho_w S_w \phi + \rho_g S_g \phi + \rho_o S_o \phi. \quad (9)$$

where the subscripts  $m$ ,  $w$ ,  $g$  and  $o$  indicate matrix, water, gas and oil,  $S$  is the fraction of saturation of each fluid component. Fluid substitution is then done using the Gassmann equation, which was given earlier in equation 2. The saturated modulus is equal to the dry modulus, as shown in equation 4. We then plug the values of the bulk and shear moduli as a function of porosity and water saturation into the equations for  $P$  and  $S$ -wave velocity given by equations 5 and 6. From equations 5, 6 and 9 we can then compute the  $V_P/V_S$  ratio and the P-impedance.

Figure 5 shows the computation of a set of curves in which we varied porosity and saturation using the following parameters:  $K_m = 36.8$  GPa and  $\mu_m = 44$  GPa (which implies that  $\nu_m = 0.073$ ),  $n = 8.64$ , and  $P = 0.02$  GPa. For the saturation change we assumed a two phase gas-water system in which  $K_{\text{water}} = 2.92$  GPa and  $K_{\text{gas}} = 0.021$  GPa. For the density, we assumed that  $\rho_m = 2.65$  g/cc,  $\rho_{\text{water}} = 1.09$  g/cc and  $\rho_{\text{gas}} = 0.001$  g/cc.

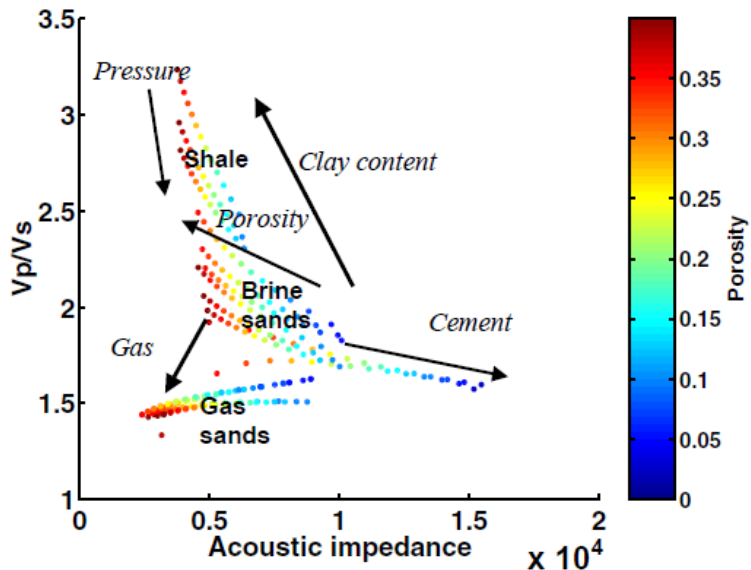


Figure 5: Cross-plot of  $V_p/V_s$  ratio versus acoustic impedance for the rock physics template using the values given in the text (Ødegaard and Avseth, 2003). A range of porosities from 5 to 40% and water saturations from 0 to 100% are shown. The colour key is fractional porosity.

The template shown in Figure 5 allows us to go back and interpret the five clusters shown in Figure 4, as shown in Figure 6.

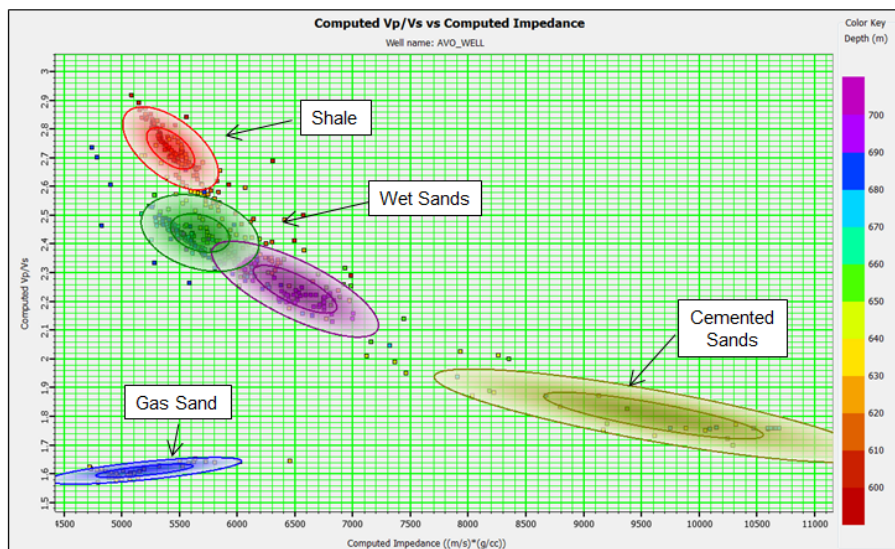


Figure 6: Interpretation of the clusters seen in Figure 4 using the rock physics template shown in Figure 5.

As seen in Figure 6, these clusters have been interpreted as shale, wet sand, gas sand and cemented sand, which corresponds to petrophysical interpretations done on the well logs.

The equations given by Ødegaard and Avseth (2003) also allow us to build two-parameter templates on top of the cross-plot, as shown in Figure 7. The template shown in this figure is given as a function of porosity and water saturation, where porosity ranges from 4 to 16% and water saturation ranges from 0 to 100%. Note that we have fit the gas sandstones, cemented sandstones and some to the wet sandstones quite well. Other rock physics templates can be built for the shale cluster.

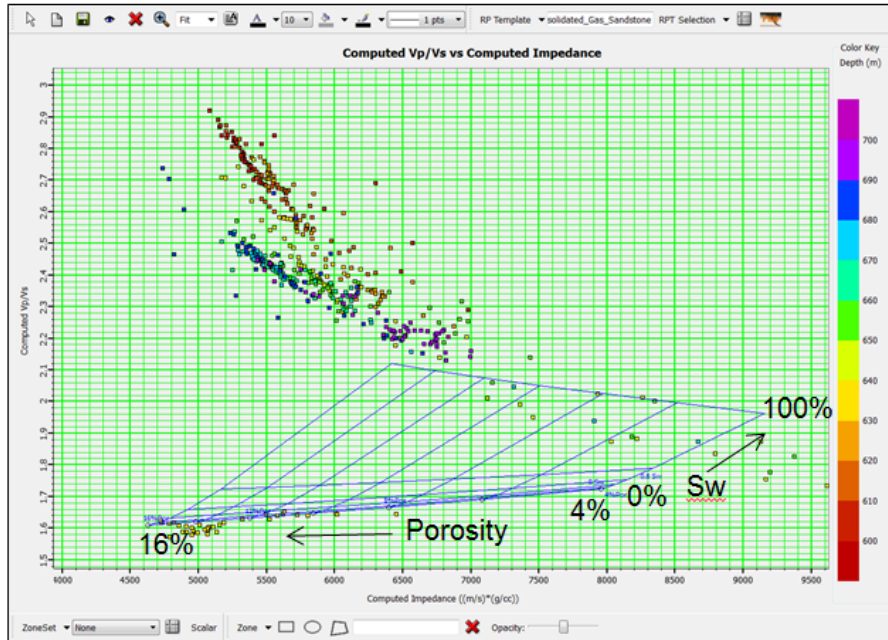


Figure 7: Superposition of set of curves created using the rock physics model of equations through on the Colony well data crossplot of Figure 3.

In the next section, we will apply the concept of the rock physics template to results extracted from the pre-stack inversion of the seismic dataset recorded around the gas well shown in Figure 1.

## THE COLONY SEISMIC DATASET AND ITS INVERSION

Figure 8 shows a small subset of CMP gathers over a seismic line that is intersects the well shown in Figure 2, as well as the resulting stack of these gathers. The gathers show a noticeable AVO Class 3 anomaly outlined around the gas sand. A class 3 anomaly is created by a sand shows a drop in both P-impedance and VP/VS ratio, which is observed both in the log curves of Figure 2 and the interpreted cross-plot of Figure 6.

The bottom part of Figure 8 shows the stack of these gathers, which forms part of an amplitude “bright spot”. Note that the information contained in the pre-stack amplitudes that suggested this was a Class 3 anomaly has been lost in the stacking process. An amplitude “bright spot” on the seismic stack could thus indicate

either a gas sand or a large amplitude from another cause, such as coal beds, which would be termed a “false” bright spot. To discriminate true gas sand bright-spots from false bright-spots was the reason that AVO analysis was first developed (Castagna et al., 1993) and many qualitative AVO techniques can be used to identify the Class 3 gas sand shown in Figure 8. However, to compare the results shown on the seismic gathers in Figure 8 with the crossplot shown in Figure 3, a more quantitative method of AVO analysis is required, one that produces elastic results.

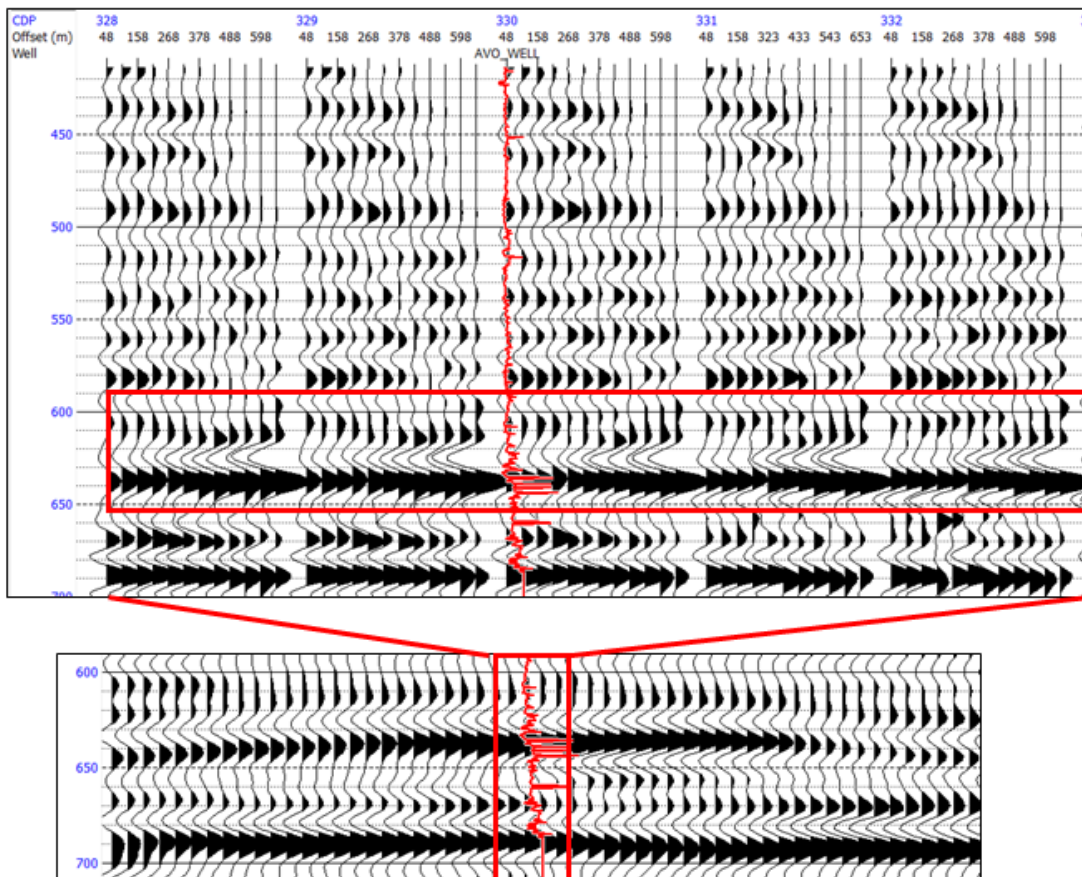


Figure 8: The top figure shows several seismic gathers around the well described in Figure 1, with a noticeable AVO Class 3 anomaly outlined around the gas sand. The bottom figure shows the stack of these gathers, which forms part of a gas sand “bright spot”.

The seismic gathers shown in Figure 8 were thus inverted using simultaneous pre-stack model-based inversion (Hampson et al., 2005), in which the output is P-impedance, S-impedance and density. Since the gathers shown in Figure 8 only contain angles out to  $30^\circ$ , the density part of the inversion is not considered reliable, so only P-impedance and S-impedance were used in the interpretation. Of course, this allows us to create the  $V_P/V_S$  ratio versus P-impedance analysis shown in Figure 3, since the ratio of the P and S impedances gives us the  $V_P/V_S$  ratio.

The result of the seismic inversion on the seismic line shown in Figure 8 is shown in Figure 9, where the colour represents  $V_P/V_S$  ratio and the wiggle-trace represents P-impedance. As expected, the gas sand anomaly in Figure 9 shows up with both low P-impedance and  $V_P/V_S$  ratio values.

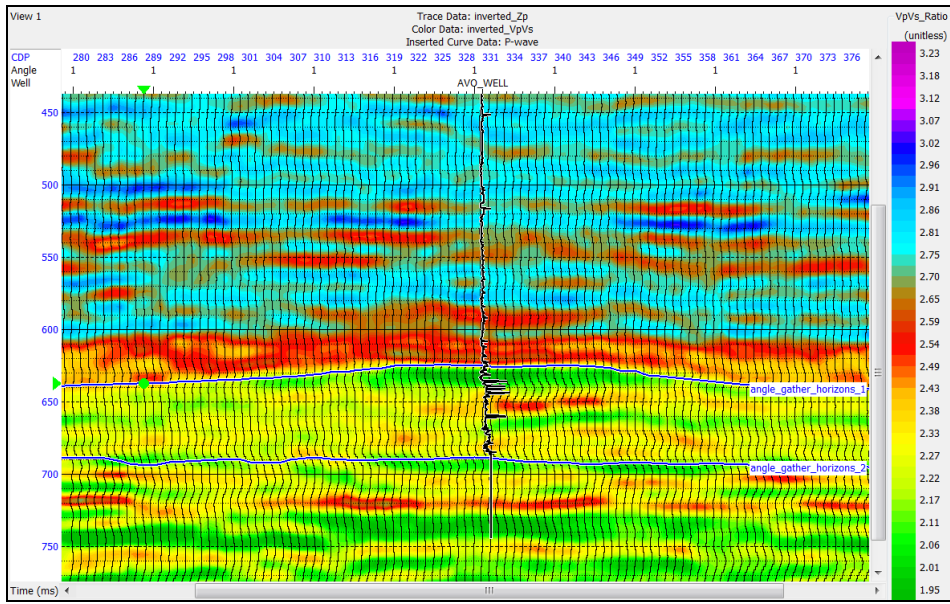


Figure 9: Pre-stack seismic inversion of the gathers shown in Figure 8, where colour represents  $V_P/V_S$  ratio and wiggle-trace represents P-impedance.

To create a cross-plot similar to that of Figure 3, we extracted P-impedance and  $V_P/V_S$  ratio from the three zones shown in Figure 10. The shallow zone, coloured blue, is from a Cretaceous sand-shale sequence, non-anomalous. The middle zone, coloured red, was picked around the gas sand itself. The deeper zone, coloured green, is from the Devonian and represents carbonates and cemented sands.

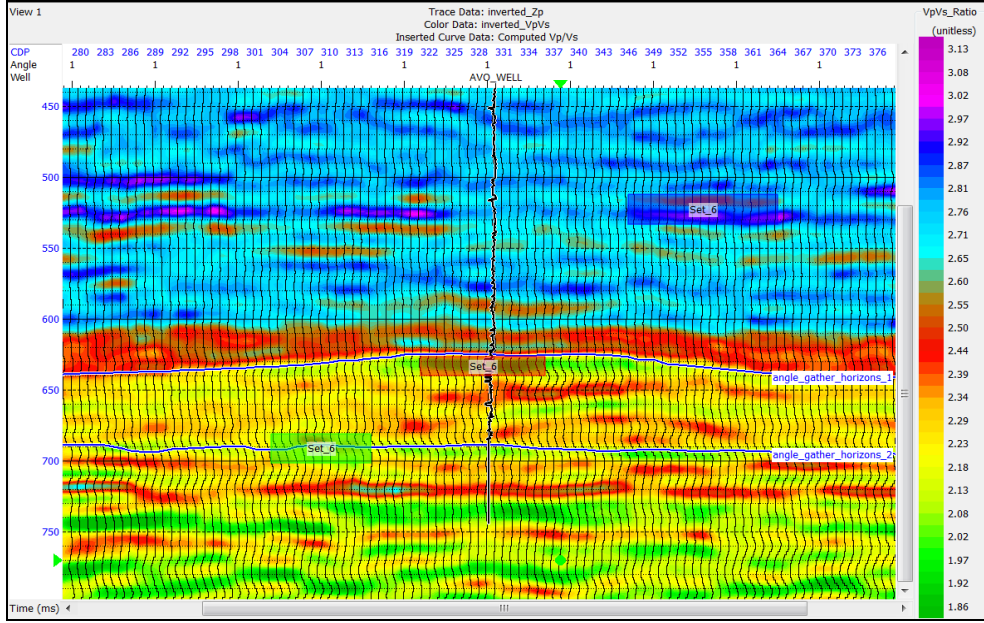


Figure 10: Three zones have been interactively picked on the dataset shown in Figure 9, where the red zone represents the gas sand, the blue zone represents wet sands and shales and the green zone represents cemented sands.

A cross-plot of the data clusters from these three zones shown in Figure 10, with  $V_P/V_S$  ratio on the vertical axis and P-impedance on the horizontal axis, is shown in Figure 11. Histograms of the three clusters are also shown on the cross-plot for

both P-impedance and  $V_P/V_S$  ratio. Note that this cross-plot can be interpreted in the same way as Figure 6, with high  $V_P/V_S$  ratio, low P-impedance shales and wet sands, low  $V_P/V_S$  ratio, low P-impedance gas sands, and medium  $V_P/V_S$  ratio, high P-impedance shales and wet sands.

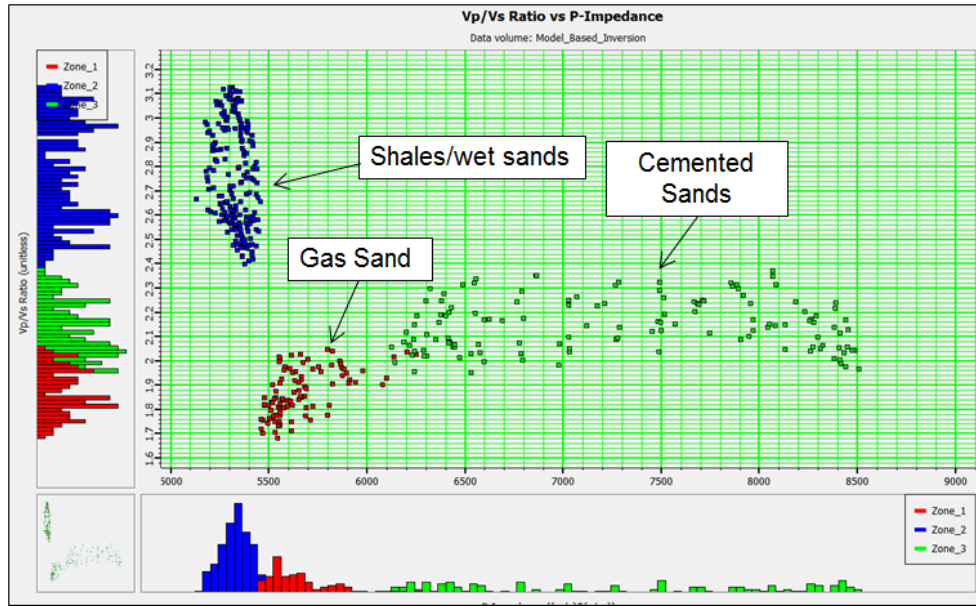


Figure 11: A cross-plot of the data clusters from these three zones shown in Figure 10, with  $V_P/V_S$  ratio on the vertical axis and P-impedance on the horizontal axis. Note the interpretation of this cross-plot from the rock physics template shown in Figure 5.

As in Figure 7, we can superimpose a rock physics template on the cross-plot shown in Figure 11. To optimize the fit, we need to modify some of the parameters that influence the template, and the values of these parameters are shown in Figure 12. Note that the effective pressure is given as the difference between the lithostatic pressure  $P_{litho}$  and pore pressure  $P_p$ .

	Minimum	Maximum	Step
Phi (fraction)	0.04	0.16	0.02
Sw (fraction)	0	1	0.2
Plitho (MPa)	70		
Pp (MPa)	65		
Vsh (fraction)	0.5	1	0.1
T (°C)	150		
Sal (kg/L)	1		
GWR (L/L)	1		
GG (unitless)	1		

Figure 12: The parameters used in the rock physics template shown in Figure 13.

The resulting rock physics template, superimposed on the cross-plot of Figure 11, is shown in Figure 13.

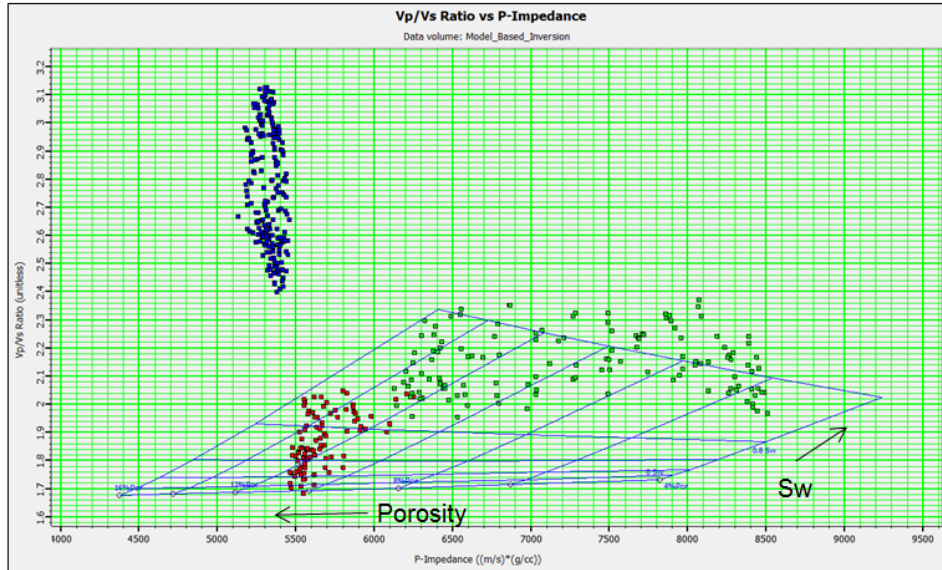


Figure 13: The rock physics template with values shown in Figure 12 applied to the cross-plot of Figure 11.

Again, the axes of this cross-plot is given by varying values of porosity and water saturation,  $Sw$ . Note that as water saturation increases, the  $V_P/V_S$  ratio also increases, but as the porosity increases the P-impedance decreases. To project the values of this cross-plot onto the seismic data, we will apply a colour scale to the template itself. This colour scale in shown in Figure 14.

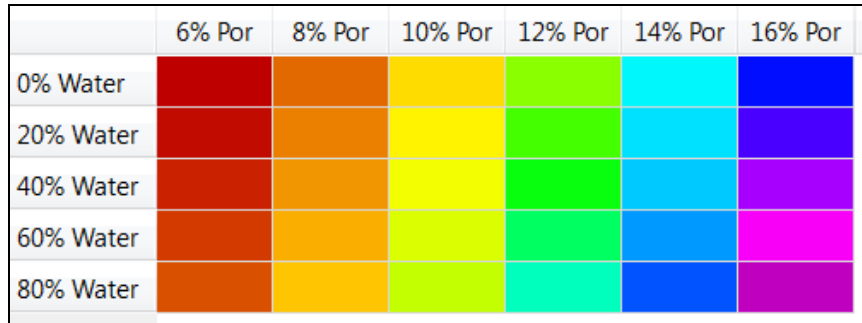


Figure 14: A rainbow-type colour palette that is applied to the rock physics template of Figure 13.

The colour scheme of Figure 14, which is the default rainbow scheme, is then applied to the rock physics template from Figure 13, as shown in Figure 15. Note that each grid cell, which is defined by porosity and water saturation increments, is thus defined by a different colour. The low porosity, low water saturation sands tend to fall into the “blue-purple” bands of colour.

Obviously, the next step is to transfer these colours to the seismic plot itself, and this is shown in Figure 16.

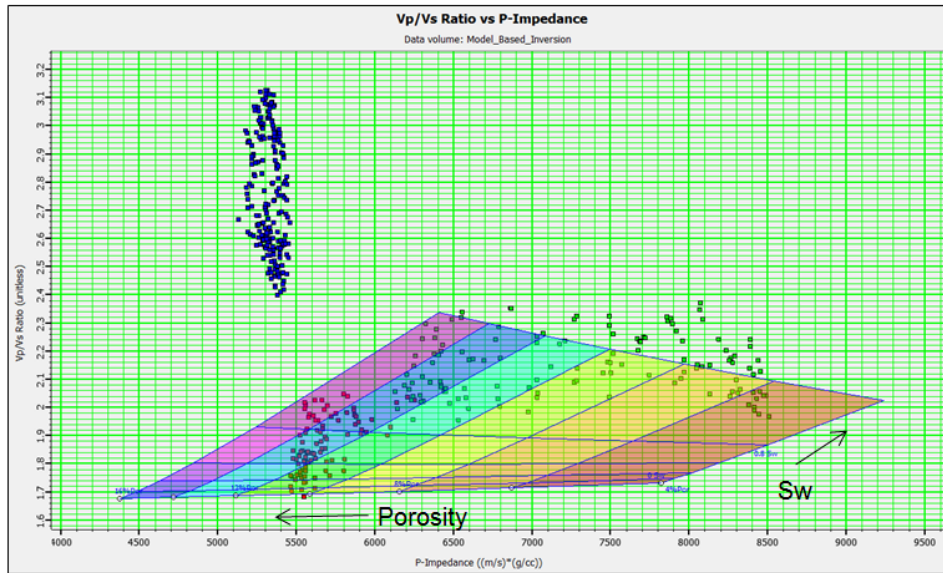


Figure 15: The colour key of Figure 14 applied to the rock physics template shown in Figure 13.

As expected, the sands associated with the zone 2 picks (the red colour) in Figure 10, are the ones that are coloured blue and purple from this new colour scheme. However, we have no clear idea where the gas sand is, since this colour scheme is quite “busy”.

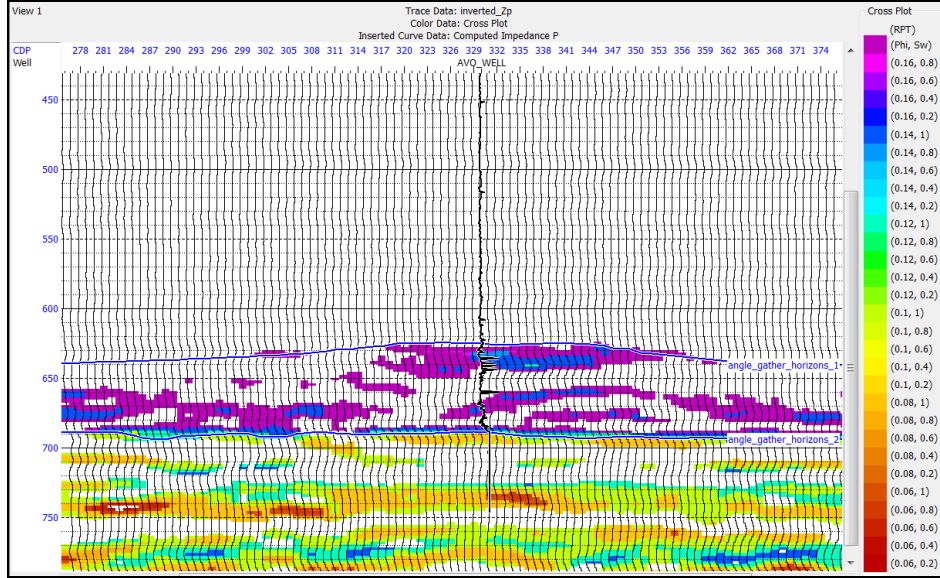


Figure 16: The colours from the rock physics template shown in Figure 15, superimposed on the seismic section from Figure 9.

I therefore went back to the colour scheme shown in Figure 12 and “cleared” it by setting all the colours to white. I then filled in certain key porosity-saturation grid cells with the colour red, as shown in Figure 17.

	6% Por	8% Por	10% Por	12% Por	14% Por	16% Por
0% Water				■		
20% Water						
40% Water						
60% Water					■	
80% Water						

Figure 17: The colour palette shown in Figure 12 after first setting all the colours to white and then highlighting key grid cells in red.

The result of applying the new colour palette shown in Figure 17 to the seismic cross-section is shown in Figure 18. Note that the gas sand anomaly now is clearly defined.

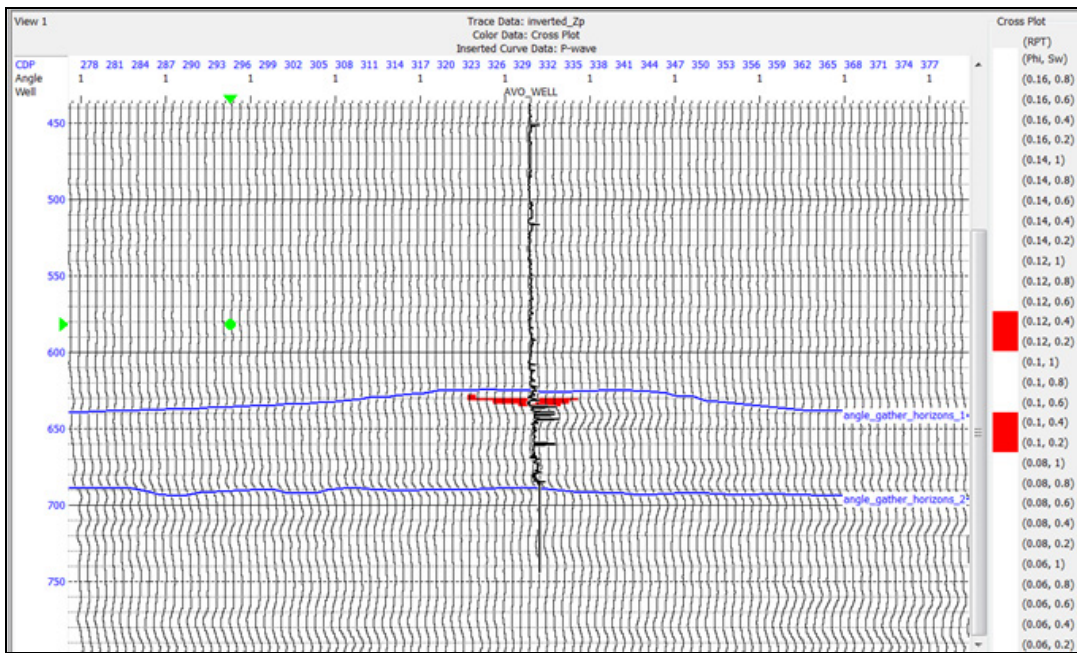


Figure 18: Application of the colour palette shown in Figure 17 to the seismic cross-section. The gas sand anomaly is now clearly identified.

In the next section, we will apply statistical methods to identify the probability of finding the gas sand in the vicinity of the region shown in Figure 18. Specifically, we will apply Bayesian classification using both bivariate Gaussian pdf and mixture-Gaussian pdf methods.

## BAYESIAN CLASSIFICATION

Now that we have analyzed the well log observations and seismic inversion results using deterministic rock physics models, we will use statistical classification methods to examine the extent of each lithology and fluid type of each of the clusters found in the seismic dataset (Theodoridis and Koutroumbas, 2009, Doyen, 2007).

The key concept in statistical classification methods is the use of probability density functions, or pdfs, to define the characteristic shape of each cluster. The most common types of pdfs are parametric, which means that they are defined by a set of parameters. And the most common type of parametric pdf is the Gaussian pdf, defined by its mean and variance. Let's start with the simplest case, a single variable. If we have  $K$  classes, or clusters, the  $k^{th}$  class can be defined by the following Gaussian pdf:

$$f(x | c_k) = \frac{1}{\sigma_k \sqrt{2\pi}} \exp\left[-\frac{1}{2}\left(\frac{x - \mu_k}{\sigma_k}\right)^2\right], \quad (11)$$

where  $\mu_k = \frac{1}{N_k} \sum_{i=1}^{N_k} x_{ki}$  represents the mean of the  $k^{th}$  class and  $\sigma_k^2 = \frac{1}{N_k} \sum_{i=1}^{N_k} (x_{ki} - \mu_k)^2$

represents the variance of the  $k^{th}$  class. We can then define a set of lines which mark the statistical boundaries between each class. In the maximum-likelihood approach we simply compute the boundary between the  $i^{th}$  and  $j^{th}$  class where the two Gaussian pdfs are equal, as follows:

$$f(x | c_i) = f(x | c_j) \quad (12)$$

In other words, equation 12 is telling us that if  $f(x | c_i) > f(x | c_j)$  we select class  $c_i$  and if  $f(x | c_i) < f(x | c_j)$  we select class  $c_j$  (Doyen, 2007).

However, implicit in equation 12 is the assumption that the two pdfs have equal weights, or priors. In the Bayesian approach, we assign different weights to each class, as shown here

$$f(x | c_i)p(c_i) = f(x | c_j)p(c_j), \quad (13)$$

where  $p(c_i)$  and  $p(c_j)$  are called the priors (Doyen, 2007).

In general, the priors are calculated by dividing the total number of points for all classes and computing the prior weight for each class by dividing the number of points in that class by the total number of points. Note that this means that the weights will add to one. Figure 19 shows the difference between the ML and Bayesian decision boundaries for a dataset taken from North Africa, using two classes. Note that the effect of including priors is to reduce the size of the pdf of the cluster with the smaller prior, and thus shift the decision boundary in the direction of this cluster.

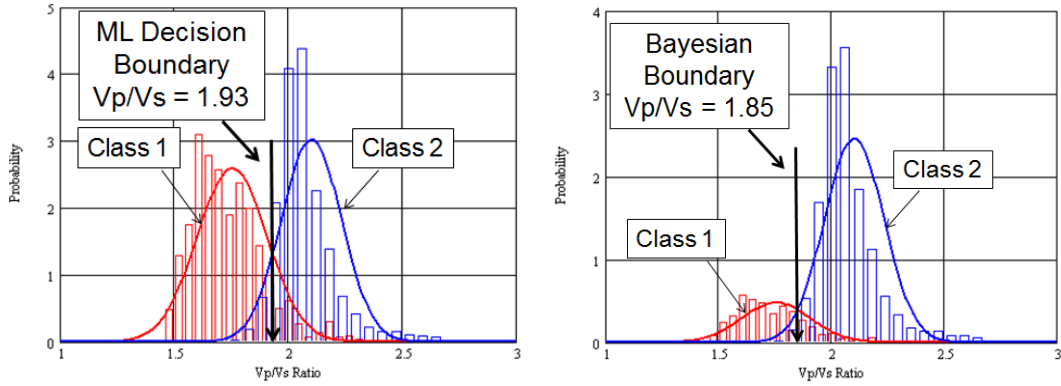


Figure 19: Decision boundaries between the  $V_p/V_s$  ratio distributions of two different clusters for a North African well example, where the ML decision boundary is shown on the left and the Bayesian decision boundary on the right.

When we extend the clusters to two dimensions, we can write the bi-variate Gaussian pdf as

$$f(x, y|c_k) = \frac{1}{2\pi|\Sigma_k|^{1/2}} \exp\left[-\frac{1}{2}(\vec{x} - \vec{\mu}_k)^T \Sigma_k^{-1} (\vec{x} - \vec{\mu}_k)\right], \quad (14)$$

where  $\vec{x} = \begin{bmatrix} x \\ y \end{bmatrix}$  is a vector containing the  $x$  and  $y$  measurements at a particular sample,

$\vec{\mu}_k = \begin{bmatrix} \mu_{kx} \\ \mu_{ky} \end{bmatrix}$  is a vector containing the means of the  $x$  and  $y$  values in the  $k^{\text{th}}$  cluster,

and  $\Sigma_k = \begin{bmatrix} \sigma_{kxx} & \sigma_{kxy} \\ \sigma_{kxy} & \sigma_{kyy} \end{bmatrix}$  is the covariance matrix which contains the variances of the  $x$  and  $y$  data values in the  $k^{\text{th}}$  cluster,  $\sigma_{kxx}$  and  $\sigma_{kyy}$ , on the main diagonal, and the

covariance of the  $k^{\text{th}}$  cluster,  $\sigma_{kxy} = \frac{1}{N_k - 1} \sum_{i=1}^{N_k} [(x_i - \mu_{kx})(y_i - \mu_{ky})]$ , on the off-diagonals. Equation 14 is the equation for an ellipse. Note that equation 14 can be extended to a multi-variate distribution of any dimension, which results in an ellipsoid in three dimensions and a hyper-ellipsoid in more than three dimensions.

Table 1 shows the bivariate statistics for the three cluster zones shown in Figure 11.

Parameters	Value	Parameters	Value	Parameters	Value
$x$ mean	5658 m/s	$x$ mean	5322 m/s	$x$ mean	7288 m/s
$y$ mean	1.87	$y$ mean	2.77	$y$ mean	2.148
$x$ variance	29341	$x$ variance	4825	$x$ variance	627481
$y$ variance	0.0091	$y$ variance	0.043	$y$ variance	0.011
covariance	9.316	covariance	-33.93	covariance	5.402

Table 1: The statistics for the three clusters shown in Figure 11, which correspond to the red cluster on the left, the blue cluster in the middle and the green cluster on the right.

Using the statistics shown in Table 1, we then compute the bivariate distributions given in equation 13, for each of the three clusters, and superimpose these elliptical surfaces on the points, as shown in Figure 20. Each ellipse represents the points contained within a single standard deviation from the mean. Note that we have gone out to two standard deviations but could have added more. Also note that we have superimposed the univariate distributions on top of the histograms shown in the figure. On those distributions it is easy to see where the decision boundaries occur.

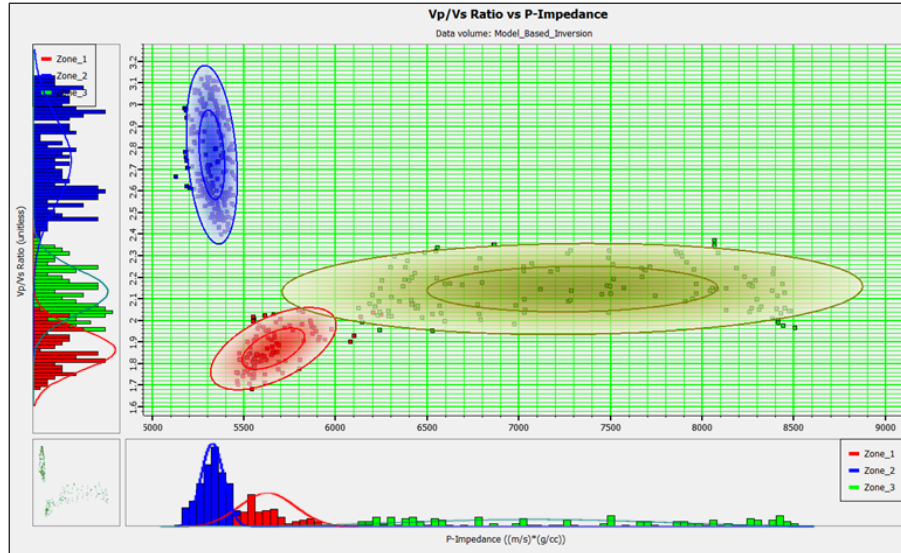


Figure 20: Bivariate elliptical Gaussian pdfs computed from the statistics in Table 1 and superimposed on the clusters of Figure 11, where each contour represents a single standard deviation.

Next, we superimpose the bivariate Gaussian distributions shown in Figure 20 back onto the seismic cross-section, as shown in Figure 21.

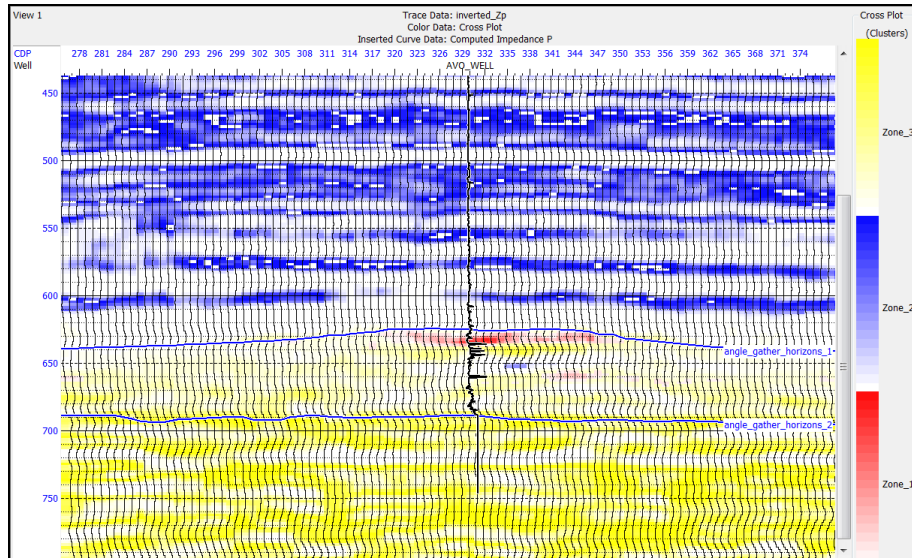


Figure 21: The distributions shown in Figure 21 superimposed on the seismic cross-section.

The colour scheme shown in Figure 21 can be interpreted as follows by referring to both the bivariate and univariate distributions shown in Figure 20. The strongest colour represents the peak on the bivariate distribution, which occurs at the mean value of each cluster. The colours are then scaled down to white based on distance from the peak, until the decision boundary is reached. When the decision boundary is reached, the colour on the scale changes to the next cluster colour.

Next, we will extend our discussion to the mixture-Gaussian approach. In this approach, each cluster is modeled as the sum of  $J$  Gaussian pdf functions, given by

$$p(x, y | c_k) = \sum_{j=1}^J w_j f(x, y | j), \quad (15)$$

where the  $w_j$  represent the weights on each individual pdf function,  $\sum_{j=1}^J w_j = 1.0$  and

$$\iint_{x,y} f(x, y | j) dx dy = 1.0. \quad \text{Table 2 shows the three Gaussian pdfs that went into a}$$

mixture model for the first cluster in Figure 11. (We will not show the mixture models for the other two clusters since by showing one result we get the point across.) Note that the mixture weights are all very close to 1/3.

	Mixture 1	Mixture 2	Mixture 3
Mixture weight	0.3298	0.3319	0.3382
x mean	5572	5565	5832
y mean	1.827	1.869	1.918
x variance	5815	3197	31002
y variance	0.0056	0.0098	0.0073
covariance	4.347	2.350	8.551

Table 2: The statistics for the three Gaussian pdfs in the mixture model for cluster 1.

The three pdfs shown in Table 2 are summed to produce the mixture-model for the first cluster, which is shown in Figure 22, as are the mixture models of the other two clusters. Again, note that the univariate distributions have been superimposed on top of the histograms shown in the figure. On those distributions it is clear that we now do not have a single Gaussian function, but instead have a mixture of three. The choice of the number of pdfs to use in the mixture is controlled by the user. Obviously, as the number of pdfs increases, the fit to the cluster gets tighter. However, including too many pdfs in the mixture can lead to “over-fitting”, in which noise or spurious points are fit too closely. Experience has shown that the use of three pdfs in the mixture is a reasonable choice.

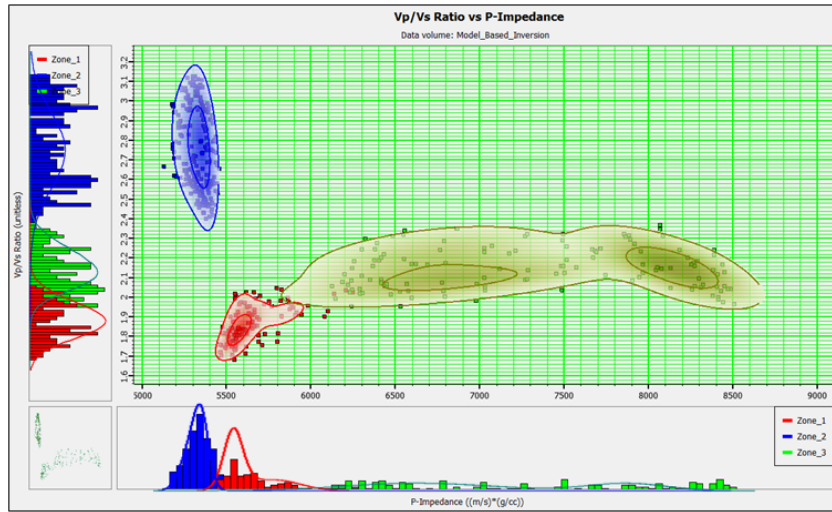


Figure 22: Mixture-Gaussian pdfs superimposed on the clusters of Figure 11, where each contour represents a single standard deviation.

Finally, we project the mixture-Gaussian pdf functions shown in Figure 22 back onto the seismic cross-section, as we did in Figure 21 for the single bivariate Gaussian pdf functions. This is shown in Figure 23. As in Figure 21, the colour scheme shown in Figure 22 can be interpreted as follows by referring to both the bivariate and univariate distributions shown in Figure 22. The strongest colour represents the peak on the bivariate distribution. However, unlike in the case of a single bi-variate Gaussian, there are multiple peaks and valleys shown in the mixture-Gaussian case. Thus, when the colours are then scaled down to white based on distance from the highest peak on the distribution, there will be multiple regions of the distribution that get that colour, not just a level surface based on a single ellips. As in Figure 20, when the decision boundary is reached, the colour on the scale changes to the next cluster colour.

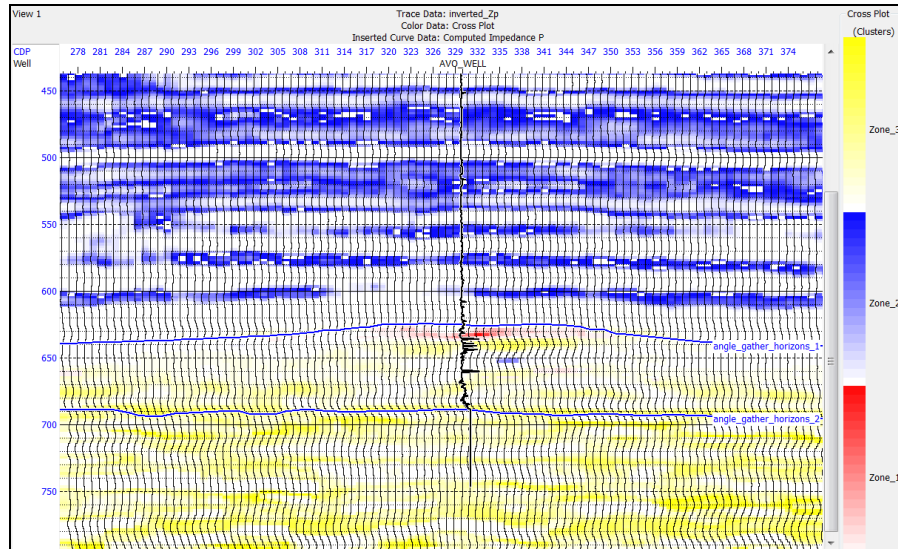


Figure 23: The distributions shown in Figure 22 superimposed on the seismic cross-section.

Note that the statistical extent of the gas sand in Figure 23 is less than its extent in Figure 22, which is probably related to the extra complexity added by the mixture Gaussian approach. Which analysis you prefer (i.e. that of Figure 23 or 24) depends on which statistical fit you believe more.

## CONCLUSIONS

In this report, I discussed several new approaches allowing us to link a rock physics template to pre-stack seismic inversion. In the first part of the talk I reviewed the theory behind the deterministic rock physics template approach, specifically for an unconsolidated gas sand model. I then showed how we could project the results of rock physics modeling onto a cross-plot of  $V_p/V_s$  ratio versus P-impedance that has been extracted from the results of simultaneous pre-stack seismic inversion. From this cross-plot interpretation we then projected the results directly onto the seismic volume itself. Having identified the hydrocarbon zone using this deterministic approach I then discussed a statistical clustering and classification approach applied to the data cross-plot which will allow us to develop a probabilistic interpretation of the extent of the hydrocarbon anomaly. This approach went beyond the normal approach using bivariate Gaussian pdf functions and introduced the concept of mixture-Gaussian pdfs. As with the deterministic method, the pdf classification functions were then projected onto the seismic volume. I illustrated all of these approaches with a gas sand example from a shallow gas field in Alberta.

## REFERENCES

- Batzle, M., and Wang, Z., 1992, Seismic properties of fluids: *Geophysics*, **57**, 1396-1408.
- Castagna, J. P., Batzle, M. L., and Eastwood, R. L., 1985, Relationships between compressional-wave and shear-wave velocities in clastic silicate rocks, *Geophysics*, **50**, 571-581.
- Castagna, J. P., Batzle, M. L. and Kan, T. K., 1993, Rock physics - The link between rock properties and AVO response, *in* Backus, M. M., Ed., Offset-dependent reflectivity - theory and practice of AVO analysis: SEG, 135-171.
- Doyen, P.M., 2007, Seismic Reservoir Characterization: An Earth Modelling Perspective: Education Tour Series, EAGE Publications bv.
- Gassmann, F., 1951, Über die Elastizität poröser Medien: *Vierteljahrsschrift der Naturforschenden Gesellschaft in Zurich*, **96**, 1-23.
- Greenberg, M.L. and Castagna, J.P., 1992, Shear-wave estimation in porous rocks: Theoretical formulation, preliminary verification and applications: *Geophysical Prospecting* **40**, 195-209.

Hampson, D.P., Russell, B.H., and Bankhead, B., 2005, Simultaneous inversion of pre-stack seismic data: SEG, Expanded Abstracts, 1633-1637.

Mavko, G., Mukerji, T., and Dvorkin, J., 1998, The Rock Physics Handbook – Tools for seismic analysis in porous media: Cambridge University Press.

Mindlin, R.D., 1949, Compliance of elastic bodies in contact: *J. Appl. Mech.*, **16**, 259-268.

Ødegaard, E. and Avseth, P., 2003, Interpretation of Elastic Inversion Results Using Rock Physics Templates: EAGE, Expanded Abstracts, E17.

Theodoridis, S. and Koutroumbas, K., 2009, Pattern Recognition, Fourth Edition: Academic Press, Elsevier.

#### **ACKNOWLEDGEMENTS**

I want to thank my colleagues at the CREWES Project and at CGG and Hampson-Russell for their support and ideas, as well as the sponsors of the CREWES Project.